Investigation of the thermal stability of MoO_x as hole-selective contacts for Si solar cells

Tian Zhang, Chang-Yeh Lee, Yimao Wan, Sean Lim, and Bram Hoex

Citation: Journal of Applied Physics **124**, 073106 (2018); doi: 10.1063/1.5041774
View online: https://doi.org/10.1063/1.5041774
View Table of Contents: http://aip.scitation.org/toc/jap/124/7
Published by the American Institute of Physics

Articles you may be interested in

Requirements for efficient hole extraction in transition metal oxide-based silicon heterojunction solar cells
Journal of Applied Physics **124**, 085702 (2018); 10.1063/1.5045250

Carrier-selective interlayer materials for silicon solar cell contacts
Journal of Applied Physics **123**, 143101 (2018); 10.1063/1.5020056

23% efficient p-type crystalline silicon solar cells with hole-selective passivating contacts based on physical vapor deposition of doped silicon films
Applied Physics Letters **113**, 061603 (2018); 10.1063/1.5037610

Analysis of pressure diffusion-wave fields in matrix-fracture media using Green functions of frequency domain
Journal of Applied Physics **124**, 074902 (2018); 10.1063/1.5040667

Estimating complete band diagrams of non-ideal heterointerfaces by combining ellipsometry and photoemission spectroscopy
Journal of Applied Physics **124**, 085302 (2018); 10.1063/1.5034774

Dynamic acousto-elastic response of single fatigue cracks with different microstructural features: An experimental investigation
Journal of Applied Physics **124**, 075303 (2018); 10.1063/1.5036531

JOURNAL OF APPLIED PHYSICS **124**, 073106 (2018)

Investigation of the thermal stability of MoO_x as hole-selective contacts for Si solar cells

Tian Zhang,[1] Chang-Yeh Lee,[1] Yimao Wan,[2] Sean Lim,[3] and Bram Hoex[1,a)]

[1]*School of Photovoltaic and Renewable Energy Engineering, UNSW Sydney, Sydney, New South Wales 2052, Australia*

[2]*Research School of Engineering, Australia National University (ANU), Canberra, Australia Capital Territory 0200, Australia*

[3]*Electron Microscope Unit, UNSW Sydney, Sydney, New South Wales 2052, Australia*

(Received 26 May 2018; accepted 3 August 2018; published online 21 August 2018)

The stoichiometry and work function of molybdenum oxide (MoO_x) are of crucial importance for its performance as hole selective contact for crystalline silicon solar cells. Hydrogenated amorphous silicon (a-Si:H) is typically used as an interface passivation layer in combination with MoO_x to reduce surface recombination. As the fabrication process of a solar cell typically contains subsequent high-temperature processes, the consideration of thermal stability of MoO_x with and without a-Si:H becomes critical. In this work, *in situ* x-ray spectroscopy (XPS)/ultraviolet photoelectron spectroscopy and Fourier transform infrared spectroscopy in the temperature range from 300 K to 900 K are used to investigate the thermal stability of MoO_x with and without a-Si:H. In addition, both the passivation and contact performance are studied by evaluating the surface saturation current density J_{0s}, carrier lifetime τ_{eff}, and contact resistivity ρ_c. The XPS results reveal that the as-evaporated MoO_x on top of both c-Si and a-Si:H is sub-stoichiometric, and the work function of both films is higher than 6 eV. While after *in situ* annealing, the evolution of MoO_x phase on top of a-Si:H shows a different behavior compared to it on c-Si which is attributed to H diffusion from a-Si:H after 600 K, whereas the work function shows a similar trend as a function of the annealing temperature. The J_{0s} of a *p*-type Si symmetrically passivated by MoO_x is found to be 187 fA/cm^2 and the ρ_c is ~82.5 mΩ·cm^2 in the as-evaporated state. With a-Si interface passivation layer, J_{0s} is significantly lower at 5.39 fA/cm^2. The J_{0s} and the ρ_c increase after post-deposition annealing. The evolution of these functional properties can be attributed to the material properties. *Published by AIP Publishing.* https://doi.org/10.1063/1.5041774

I. INTRODUCTION

Traditional carrier selective contacts for crystalline silicon (c-Si) solar cells use highly doped silicon regions to effectively separate and extract light generated carriers. Higher carrier selectivities can be obtained by using a thin tunneling oxide in combination with polycrystalline silicon (poly-Si) or a stack of intrinsic and doped hydrogenated amorphous silicon (a-Si:H), and these types of contacts have enabled silicon solar cell efficiencies above 25% in recent years. However, these contacts have drawbacks, such as enhanced Auger recombination, parasitic absorption, and low thermal stability, which restrict their application.[1–3] To avoid these drawbacks and push the efficiency further to the efficiency limit of silicon solar cells, transition metal oxides (TMOs) are widely studied as alternative carrier selective materials. These TMOs usually have an extreme high or low work-function relative to silicon which results in significant band bending in the silicon to assist the collection of one particular polarity (electrons or holes).[4] For example, high work function (>6 eV) TMOs can move the Fermi level in c-Si close to the valence band, which aids the extraction of holes and blocks the electrons. Therefore, they provide an efficient way for the collection of holes and reduce the carrier recombination significantly, vice versa, for electron selective metal oxides with very low work functions. Initially adopted in organic or perovskite solar cells, molybdenum oxide (MoO_x),[5,6] tungsten oxide (WO_x),[7,8] vanadium oxide (VO_x),[9,10] and chromium oxide (CrO_x)[11] have shown excellent optical and electronic properties to work as a hole collector. More recently, researchers have started to investigate the application of these oxides as hole selective contacts on silicon-based solar cells. Among these high work function TMOs, MoO_x is the most extensively studied.[12–16] It is generally accepted that oxygen vacancies in MoO_x act as n-type dopants which contribute to its electronic properties, and high oxygen vacancies can form new stable oxidation state of the cation. Therefore, the oxygen vacancy density in MoO_x is critical for its application.[17] Most studies have shown that as-prepared thermal evaporated MoO_x is sub-stoichiometric ($x < 3$) and has a high work function of >6 eV.[14,18] Thermal evaporated MoO_x can achieve a relatively low contact resistivity ρ_c of 1 mΩ·cm^2 on p-type silicon wafers and the contact saturation current density is found to be ~300 fA/cm^2 on n-type silicon,[16] which is promising for its application as the hole selective contact. Battaglia *et al.*[13] managed to achieve an open circuit voltage of 711 mV and an efficiency of 18.8% using a thermal evaporated MoO_x hole selective layer in combination with an a-Si:H interface passivation layer. More recently, an efficiency of 22.5% was

a)Electronic mail: b.hoex@unsw.edu.au

obtained for a solar cell with a MoO_x as the hole selective contact.[19] Except for thermal evaporation, other popular techniques for synthesizing MoO_x thin films include atomic layer deposition (ALD),[20,21] radio frequency (RF) sputtering,[22] and solution processing.[23] However, the performance of MoO_x films prepared by these techniques is still inferior compared with films prepared by thermal evaporation.

On the other hand, the thermal stability of thermal evaporated MoO_x is rarely studied, although it is critical during the fabrication process of solar cells. For example, the transparent conductive oxide (TCO) layer which usually is applied to increase the lateral conduction is typically annealed to obtain optimal conductivity,[15,24,25] which makes it important to take the thermal stability of TMOs into consideration. There are studies indicating that the performance of MoO_x based solar cells degrades after annealing, e.g., the fill factor of SHJ solar cells dropped from 76.6% to 69.7% after stepwise annealing from 130 °C to 200 °C[19] or the efficiency decreased from 12.6% to 11% after 160 °C annealing of the solar cell,[26] yet no detailed analysis was done to show the cause of this degradation.

In this work, we use *in situ* x-ray/ultraviolet photoelectron spectroscopy (XPS/UPS) to study the material properties of thermal evaporated MoO_x during post-deposition annealing. The MoO_x films were deposited directly on top of c-Si or with an interface a-Si:H passivation layer. In combination with Fourier Transform Infrared (FTIR) spectroscopy analysis, the material properties of thermal evaporated MoO_x, such as the film stoichiometry, work function, and the interface evolution, will be studied after annealing at different temperatures. Furthermore, the surface saturation current density J_{0s}, carrier lifetime τ_{eff}, and contact resistivity ρ_c of the films are also studied and further explained by the material properties derived from the XPS/UPS and FTIR.

II. EXPERIMENTAL

~280 μm thick 4 Ω·cm *p*-type float-zone (FZ) c-Si wafers were used for material analysis and surface passivation experiments. Prior to deposition, all wafers went through a standard RCA (Radio Corporation of America) cleaning process and were dipped in 2% w/v HF solution to remove the native silicon oxide. The MoO_x films were deposited by thermally evaporating molybdenum (VI) oxide powder (99.97% purity, Sigma Aldrich) using a commercial evaporator (Daedong Hightechnologies, Solar-Dual Bridge). A-Si:H was deposited by plasma enhanced chemical vapor deposition (PECVD, Oxford Plasmalab System 100) at 300 °C. The sample without and with a-Si will be referred to as MoO_x/c-Si and MoO_x/a-Si sample in the remaining part of this article.

The film thickness was determined by spectroscopic ellipsometry (SE, M-2000VI, JA Woollam). The cross-sectional nanostructure and elemental distribution across the c-Si/MoO_x interface were detected using a JEOL JEM-ARM200F (200 kV) aberration-corrected scanning transmission electron microscopy (STEM) equipped with an energy dispersive x-ray spectroscopy (EDS) system. XPS was performed to investigate the film stoichiometry, while UPS was used to extract the work function. The molecular bond composition of the films was analyzed by FTIR. XPS was done with a Thermo Scientific ESCALAB 250Xi spectrometer, using monochromatic Al Kα X-ray source with an energy of 1486.68 eV. The system was also equipped with a He discharge lamp for UPS (He I at hν = 21.2 eV and He II at hν = 40.8 eV). The background vacuum in the measuring chamber was lower than 2×10^{-9} mbar. The measurement spot size was 500 μm. The samples were loaded into the XPS chamber directly after deposition to avoid excessive contamination by ambient exposure. After the desired background pressure was obtained, the measurement was carried out at room temperature (300 K). Then, the sample was heated stepwise from 300 K to 900 K with an increment of 100 K. XPS/UPS data were collected at each temperature. Ar^+ ion sputtering is normally used to clean the sample surface before XPS/UPS measurement. However, as the previous work indicated that Ar^+ ion sputtering can induce the unintentional reduction of the oxidation state of Mo,[27,28] this cleaning was not performed in this work. This potentially results in a higher surface contamination of the sample and is taken into account in the analysis of the measurements. As a complementary analysis, FTIR was performed to further investigate the composition of the thermal evaporated films. The FTIR (Thermo Fisher Nicolet 5700) measurements were done in transmission mode. The absorption spectra of the films were obtained by comparing the sample's IR transmission before and after the deposition. A sample holder at Brewster's angle (~74°) with a *p*-type polarizer was used to eliminate the impact of interference in the c-Si substrate on the measurement. Symmetrical structures were used for the FTIR analysis to improve the signal-to-noise ratio and in addition ensured that the oxidation or contamination at the uncoated side did not affect the measurement. Both samples were measured at room temperature first, following which they were annealed in 5000 sccm N_2 gas in a rapid thermal process system (Modular Process Technology RTP-600xp) from 400 K to 900 K for 10 min at each temperature. After each annealing step, an FTIR measurement was taken. The effective minority carrier lifetime τ_{eff} and surface saturation current density J_{0s} of the MoO_x and a-Si/MoO_x stack before and after annealing were evaluated by quasi-steady-state photoconductance (QSSPC, Sinton WCT-120). Single side deposited samples were prepared to assess the contact resistivity using the Cox and Strack method.[29] 2 Ω·cm p-type Czochralski (Cz) Si wafers with a thickness of ~180 μm were used in this case. The structure was made by evaporating a Pd (40 nm)/Ag (300 nm) metal stack on top of MoO_x through a shadow mask with a pattern of 10 circular pads with a diameter ranging from 0.1 cm to 1 cm with 0.1 cm increment. A full area Al (~1 μm) layer was evaporated directly on the other side of c-Si. The samples were also annealed in an N_2 atmosphere from 400 K~ 900 K for 10 min. Before and after annealing, dark *I-V* (current-voltage) measurements were performed using a four-probe station.

III. RESULTS AND DISCUSSION

A. Material properties

A 9 nm MoO_x film was thermally evaporated directly on top of c-Si with or without a PECVD a-Si:H interface

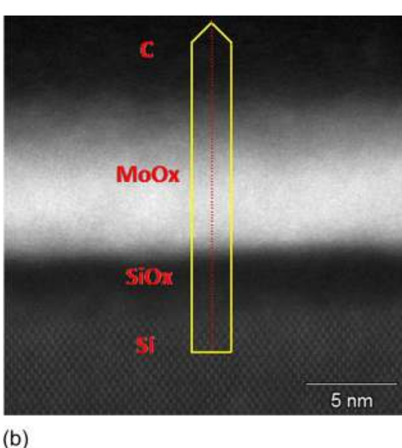

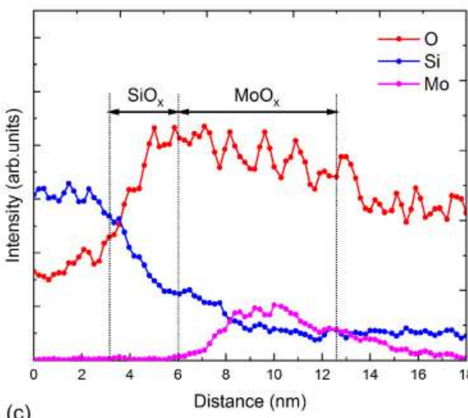

FIG. 1. (a) Bright field STEM image of the as-deposited MoO_x/c-Si sample. (b) High angle annular dark field (HAADF)–STEM image and the direction and region for EDS line scan and (c) resulting compositional distribution extracted from the EDS line scan.

passivation layer. The a-Si:H thickness used for the XPS/UPS measurement was ~9 nm, while it was ~5 nm for the other experiments. A typical STEM image of the MoO_x/c-Si sample and the corresponding EDS analysis are shown in Fig. 1. Prior to the STEM measurement, a carbon layer was deposited on top of the MoO_x film to increase the contrast in the STEM measurement. The cross-sectional image and EDS spectra reveal the presence of a SiO_x interlayer, which is commonly observed when depositing metal oxide films on top of c-Si.[30] Please note that the film thickness extracted from the STEM image was not identical to the one extracted from the SE measurements before the STEM image was obtained. The MoO_x appears to be only ~6.4 nm rather than 9 nm. This is most likely attributed to the fact that the dielectric contrast between MoO_x and SiO_x is not very large, making it challenging to differentiate between them in an ellipsometry measurement, particularly for a total film thickness of only ~10 nm. However, once the SiO_x thickness was known from the STEM image, the re-fitting of ellipsometry data revealed the same results as the STEM image. The TEM image of MoO_x/a-Si revealed an interfacial SiO_x layer with a similar thickness as the MoO_x/c-Si sample. This can be found in the supplementary material.

The XPS measurements on as-deposited samples revealed that the MoO_x films contained both the Mo^{+6} and Mo^{+5} oxidation states, which implied that the films were sub-stoichiometric. The O to Mo ratio was calculated to be ~2.86 for both the MoO_x/c-Si and the MoO_x/a-Si samples. Figure 2 shows the XPS core level spectra of Mo 3d in the MoO_x/c-Si sample before and after annealing. The deconvolution of the spectra was calibrated by referencing to the well-known adventitious hydrocarbon C 1s peak at ~284.8 eV or to the Si 2p peak at 99.4 eV when no C 1s peak was detected. A doublet of two equal-width Gaussian-Lorentzian peaks with the binding energy of Mo $3d_{5/2}$ centered at 233.1 ± 0.1 eV and Mo $3d_{3/2}$ at 236.2 ± 0.1 eV is the representative of Mo^{+6} oxidation state.[31,32] Similarly, another doublet with ~3.2 eV spin-orbit splitting represents Mo^{+5} with the Mo $3d_{5/2}$ peak centered at 231.9 ± 0.1 eV and Mo $3d_{3/2}$ at 235.1 ± 0.1 eV.[31–33] The binding energy of Mo $3d_{5/2}$ at 230.9 ± 0.1 eV is the indication of Mo^{+4}. There is also a peak doublet located at a binding energy between Mo^{+5} and Mo^{+4} which, according to Scanlon *et al.*,[34] is the result of an electron screening effect from the metallic MoO_2 phase.

From Fig. 2, it is obvious that as the annealing temperature increases, the relative intensity of the Mo^{+5} peak increases, while the Mo^{+4} peak appears at 600 K. This is clear evidence that the MoO_x film degraded gradually with the increase in the annealing temperature. Conceivably, the density of oxygen vacancies increased. The MoO_x/a-Si sample shows similar results which can be seen in the supplementary material. To further investigate the degradation mechanism of the films, the O 1s spectra was also analyzed. Four peaks were used to deconvolute O 1s spectra from the MoO_x/c-Si sample. The XPS peak of the O^{2-} state in MoO_x lattice is around 531.0 ± 0.1 eV,[35] and the peak at 532.0 ± 0.1 eV was associated with weakly bonded O^- in the subsurface of transition metal oxide.[36,37] As MoO_x is

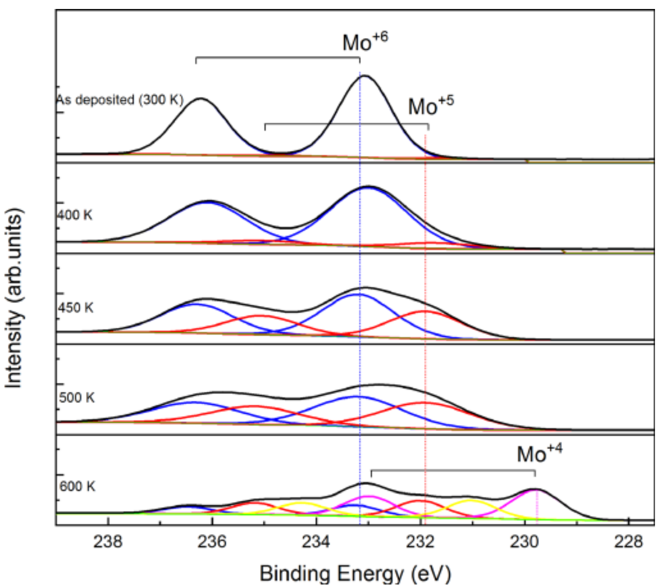

FIG. 2. XPS spectra of Mo 3d in MoO_x film at different post-deposition annealing temperatures. It can clearly be seen that Mo^{+5} peaks increase in intensity at higher annealing temperatures until after 600 K annealing where Mo^{+4} appears.

well known for absorbing water from the ambient, the peak around 532.4 ± 0.1 eV was assigned to H_2O.[38–40] In addition, the SiO_x interlayer, which was unintentionally generated on the silicon surface, was detected by XPS. Therefore, the peak at 532.9 ± 0.1 eV was attributed to the O from SiO_x.[41] For the MoO_x/a-Si sample, an additional peak should be taken into consideration,[42] which is related to hydroxyl groups at a peak position of 531.5 ± 0.1 eV due to H diffusion from the a-Si:H interface passivation layer at high temperatures.[38,43] Figure 3 shows the O 1s core level spectra of the two samples. It is obvious that the signal from SiO_x and/or OH^- was not prominent in the as-prepared films. Except from the difference due to the absorbance of H_2O, the relative O density is roughly the same for both samples. The relative share of the three different oxidation states of Mo, i.e., Mo^{+6}, Mo^{+5}, and Mo^{+4} is shown in Fig. 4. For both samples, the Mo^{+6} related peak keeps decreasing with the increase in the temperature, and the Mo^{+5} related peak intensity first increases and then decreases when Mo^{+4} appears. However, in the MoO_x/c-Si sample, Mo^{+4} appears at 600 K, while it appears at 700 K in the MoO_x/a-Si sample. It seems that the presence of a-Si:H, more particular the release of hydrogen, influences the stability of the MoO_x film.

On the other hand, the analysis of oxygen states revealed that the O^{2-} in the structural MoO_x decreases with the increase in the temperature, while the unstable O^- oxidation state increases. This is consistent with our previous work done on WO_x films.[42] The signal from SiO_x increases for both samples as illustrated in Fig. 5 possibly due to oxygen consumption by the underlying Si. A similar result was observed for AlO_x films grown directly on c-Si.[44] It is interesting to note that the oxygen consumption in the MoO_x/a-Si appears to be slower compared to the MoO_x/c-Si sample for annealing temperatures below 700 K. This could potentially be attributed to the presence of OH^- groups as shown in Fig. 5. There is a sharp increase in OH^- in the MoO_x film at 600 K, which undoubtedly is resulting from the out-diffusion of hydrogen from the a-Si:H interface passivation layer, then after 700 K annealing, the signal from SiO_x in the MoO_x/a-Si sample becomes higher when compared with the sample without a-Si. This is in good agreement with the study of Ponpon *et al.*[45] who showed that the oxidation rate of PECVD a-Si:H is slower than that of c-Si and the oxidation rate reduces with the increase in the hydrogen concentration. Besides, the decrease in OH^- concentration for annealing temperature above 600 K could be resulting from further diffusion of H which combines with OH^- in the MoO_x forming H_2O vapor which then escapes from the

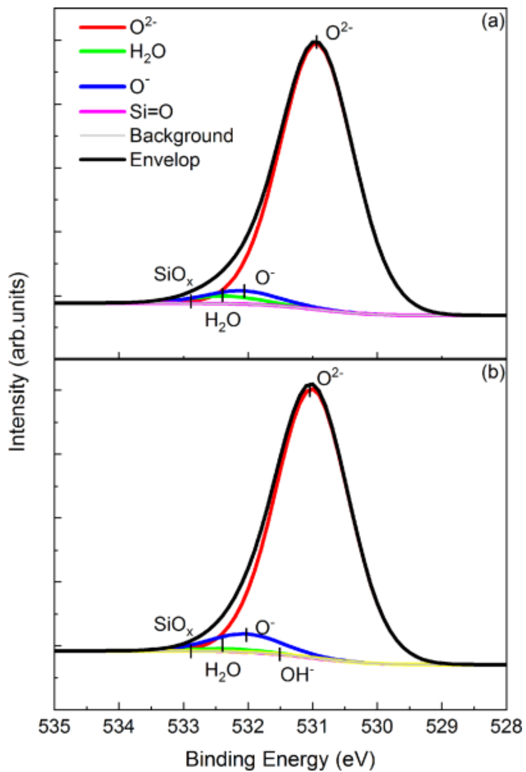

FIG. 3. O 1s spectra of (a) the MoO_x/c-Si sample and (b) the MoO_x/a-Si sample.

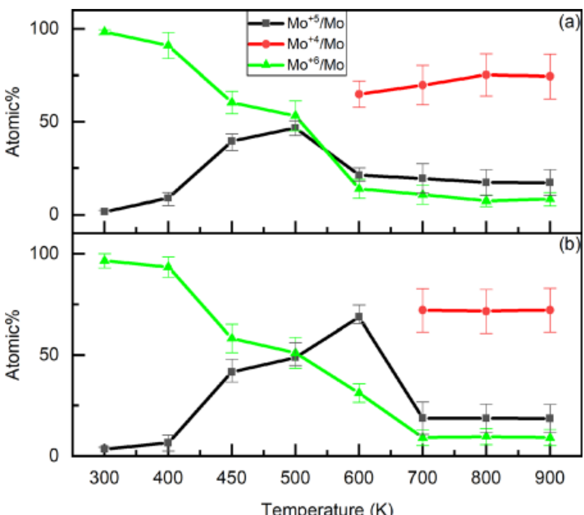

FIG. 4. Temperature-dependent relative share of different Mo oxidation states in (a) the MoO_x/c-Si sample and (b) the MoO_x/a-Si sample. The error bars are in the range of 8%–40%, considering possible errors in the fitting of XPS spectra and the calculation of the atomic percentage.

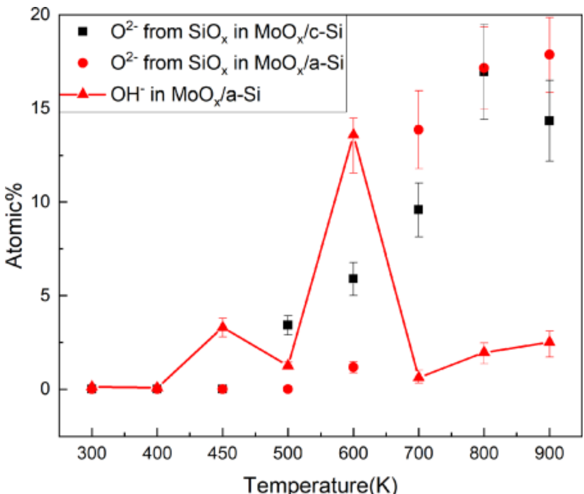

FIG. 5. Temperature-dependent SiO_x concentration for the MoO_x/c-Si and MoO_x/a-Si samples and OH- concentration in the MoO_x/a-Si sample. The error bars are in the range of 1%–45%, considering possible errors in the fitting of XPS spectra and the calculation of the atomic percentage.

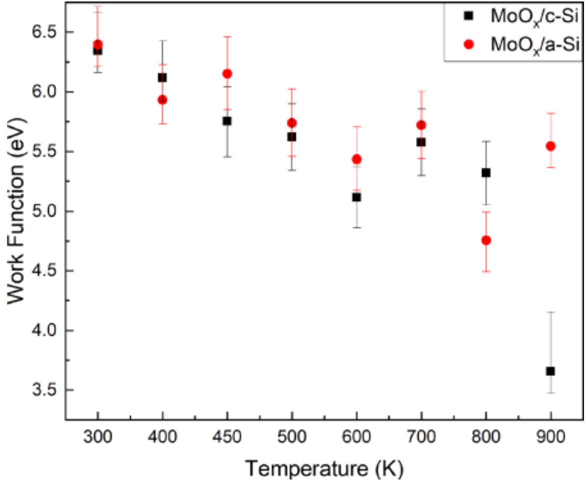

FIG. 6. Temperature-dependent work function of the MoO_x/a-Si and MoO_x/c-Si samples. The error bars are in the range of 3%–14%, considering possible errors in the fitting of UPS spectra.

films.[46] This also explains why the MoO_x/a-Si sample did not show the Mo^{+4} oxidation state until 700 K annealing as shown in Fig. 4. In all, the presence of a-Si:H suppressed the growth of the SiO_x below 600 K. It should be noted that during the XPS/UPS measurements, the contact between the samples and their holder at the 900 K set-point was unstable, thus, unfortunately, the uncertainty at this data point is significantly higher than for lower annealing temperatures.

Figure 6 shows the temperature dependent work function of the MoO_x films grown on both c-Si and a-Si. The work function keeps decreasing with the increase in the annealing temperature for both samples. Although the presence of a-Si:H improves the stability of MoO_x in terms of the Mo oxidation state, there is no such sign from the MoO_x work function. The reason could be the fact that UPS only collects information from the top 2 nm of the film while XPS collects signal from the first 10 nm. It is quite likely that there is a nonuniform distribution of H in the MoO_x film which could then explain the differences between the two measurements.

The FTIR measurements of the MoO_x/c-Si and MoO_x/a-Si samples are shown in Fig. 7. The peak at the wavenumber of 1100–1300 cm^{-1} was assigned to SiO_x.[47,48] The intensity of SiO_x related absorption peak of the MoO_x/c-Si increases for annealing temperatures $\geq$ 600 K and reaches a maximum for the highest annealing temperature. This result is in agreement with the XPS result shown in Fig. 5. However, the SiO_x from the spectra of the MoO_x/a-Si sample at 600 K annealing is not shown to be obviously thinner. The reason could be that the annealing atmosphere for FTIR samples was N_2 rather than vacuum, which could explain the differences between the FTIR and XPS measurements.

B. Passivation and contact resistivity

The as-deposited MoO_x film yielded an effective minority carrier lifetime of 211.4 μs (at an injection level of 1×10^{15} cm^{-3}) and the J_{0s} was determined to be 187 fA/cm^2 as shown in Fig. 8(a). After annealing, the lifetime started to decrease and kept decreasing with the increase in the annealing temperature. When the temperature reached 450 K, the J_{0s} could no longer be extracted from the measurement due to high carrier recombination at high injection level. On the other hand, the a-Si/MoO_x stack undoubtedly showed better passivation with a J_{0s} value of only 5.39 fA/cm^2, but this also significantly increased for annealing temperatures >500 K. It is also noticeable that the 450 K (∼180 °C) annealing did not improve the effective lifetime of the sample although the J_{0s} reaches to its minimum 4.22 fA/cm^2, while this temperature is normally well known to improve the chemical passivation of a-Si:H. It could be that in this case the improvement in chemical passivation for the a-Si:H was compensated by the degradation of the MoO_x film.

Dark *I-V* (current-voltage) results for the evaluation of the contact performance are shown in Fig. 9. The MoO_x films on bare Si generated good ohmic contact performance, which illustrates that the holes can be conducted smoothly through this structure. Unfortunately, the structure with a-Si only gave a Schottky junction performance (not shown). The reason could be the formation of SiO_x at the rearside of the sample during the deposition of a-Si:H. The ρ_c of MoO_x/c-Si sample calculated from the *I-V* curves was found to be ∼82.5 mΩ·cm^2. After annealing at temperatures of 400 and 450 K, this value increased to 102 mΩ·cm^2 and 606 mΩ·cm^2, respectively. For annealing temperatures ≥500 K, ρ_c became so large that this structure also showed a Schottky diode behavior. Based on the material analysis, this can be attributed to a decreasing MoO_x work function and an increase in the SiO_x thickness at the interface. Furthermore,

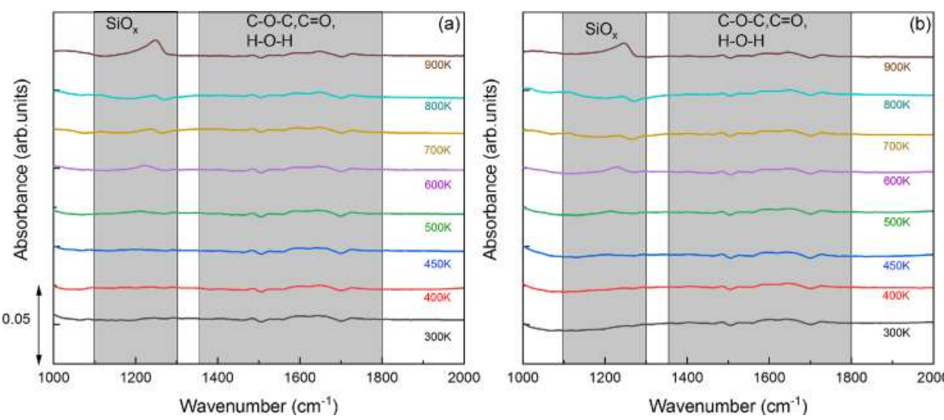

FIG. 7. Evolution of FTIR transmission spectra of the (a) MoO_x/c-Si and (b) MoO_x/a-Si after annealing in the temperature range from 300 to 900 K. The FTIR spectra were offset vertically for clarity.

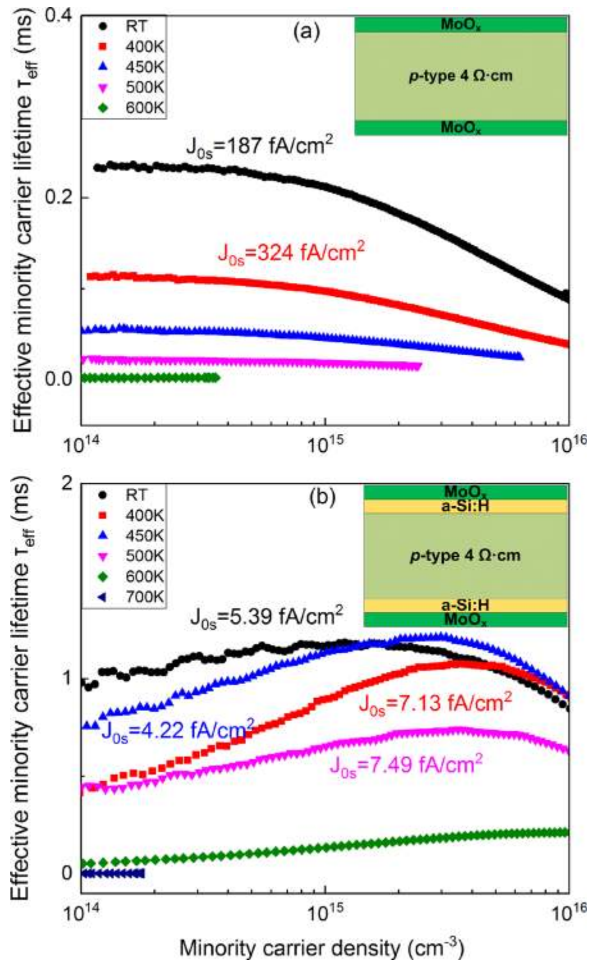

FIG. 8. Effective minority carrier lifetime and J_{0s} of a 4 Ω p-type FZ c-Si wafer symmetrically passivated by double side (a) MoO_x and (b) a-Si/MoO_x stack after various post-deposition annealing treatments.

the optimization of the contact performance of the structure with a-Si passivation layer still needs investigation.

IV. CONCLUSION

As-evaporated MoO_x was found to be sub-stoichiometric using XPS analysis, and the work function was found to be ∼6.35 eV when deposited on either a c-Si or a-Si layer surface. *In situ* annealing in a XPS/UPS chamber revealed the degradation of MoO_x, but it was found to be strongly dependent on the underlying layer. Although the thickness of the SiO_x interlayer between MoO_x and c-Si or a-Si:H was found to increase after annealing, the increase in thickness on a-Si:H was found to be lower compared to c-Si below 600 K. The work function of the MoO_x films was found to decrease for both cases. This can explain the increase in contact resistance after annealing. Although the a-Si/MoO_x stack showed better passivation to c-Si/MoO_x, both were found deteriorate after annealing. Besides, the as-evaporated MoO_x on c-Si gives a reasonably low contact resistivity of ∼82.5 mΩ·cm^2, while it was found to be too high for the sample with a-Si that it only shows a diode performance. In all, this study analyzed the thermal stability of thermal evaporated MoO_x using *in situ* XPS/UPS and FTIR in terms of material properties, which provided the degradation mechanism of MoO_x working as a hole selective contact for c-Si solar cells and gave important insights for using this novel material on higher efficiency silicon solar cells.

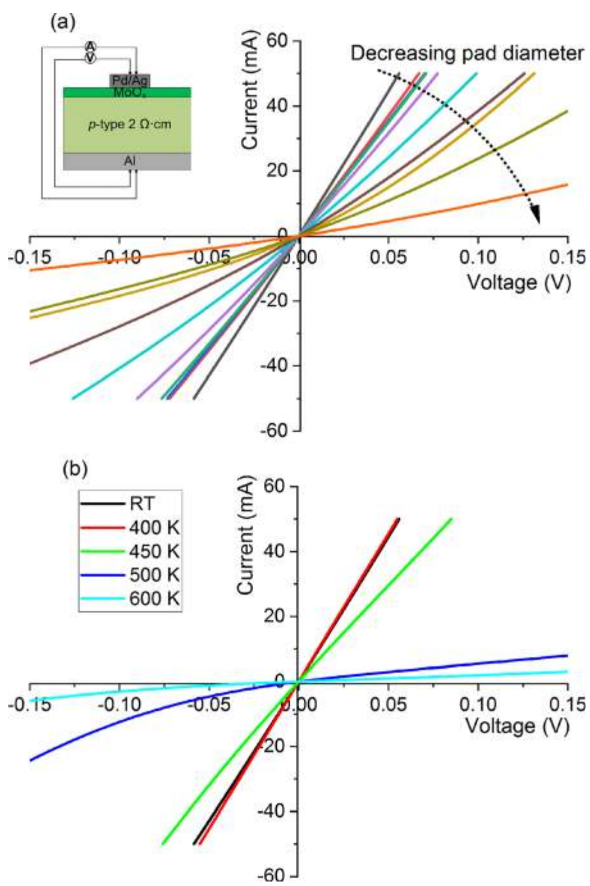

FIG. 9. Dark *I-V* measurement of the pSi/MoO_x contact structure (a) as prepared on pads of different size and (b) on the 1 cm diameter pad after different temperature annealing.

SUPPLEMENTARY MATERIAL

See supplementary material for the TEM image and FTIR results of the MoO_x/a-Si sample indicating the interfacial SiO_x and the Mo 3d core level XPS spectra evolution of the MoO_x/a-Si sample.

ACKNOWLEDGMENTS

This work was funded by the Qatar National Research Fund (a member of Qatar Foundation, NPRP Grant No. NPRP9-021–009) and by ARENA as part of ARENA's Research and Development Program – Solar PV Research (Grant No. 2017/RND007). The views expressed herein are not necessarily the views of the Australian Government, and the Australian Government does not accept responsibility for any information or advice contained herein. The authors would like to thank Outi Mustonen in the Mark Wainwright Analytical Centre, UNSW, who helped to perform the XPS measurement, and David Mitchell at the University of Wollongong (UOW) Electron Microscopy Centre for the assistance on STEM and EDS.

[1]M. A. Green, IEEE Trans. Electron Devices **31**, 671 (1984).
[2]Z. C. Holman, A. Descoeudres, L. Barraud, F. Z. Fernandez, J. P. Seif, S. De Wolf, and C. Ballif, IEEE J. Photovoltaics **2**, 7 (2012).

[3]M. J. Kerr, A. Cuevas, and P. Campbell, Prog. Photovoltaics Res. Appl. **11**, 97 (2003).
[4]P. Koswatta, M. Boccard, and Z. Holman, in *IEEE 42nd Photovoltaics Specialist Conference PVSC* (IEEE, 2015), p. 1.
[5]Y. Zhao, A. M. Nardes, and K. Zhu, Appl. Phys. Lett. **104**, 213906 (2014).
[6]S. Murase and Y. Yang, Adv. Mater. **24**, 2459 (2012).
[7]L. S. Kumar, D. P. Bhatt, and S. Karthikeyan, J. Environ. Nanotechnol. **5**, 48 (2016).
[8]Z. L. Tseng, L. C. Chen, C. H. Chiang, S. H. Chang, C. C. Chen, and C. G. Wu, Sol. Energy **139**, 484 (2016).
[9]C. P. Chen, Y. D. Chen, and S. C. Chuang, Adv. Mater. **23**, 3859 (2011).
[10]J. Meyer, K. Zilberberg, T. Riedl, and A. Kahn, J. Appl. Phys. **110**, 033710 (2011).
[11]P. Qin, G. Fang, N. Sun, X. Fan, Q. Zheng, F. Chen, J. Wan, and X. Zhao, Appl. Surf. Sci. **257**, 3952 (2011).
[12]A. G. Aberle, S. Glunz, and W. Warta, J. Appl. Phys. **71**, 4422 (1992).
[13]C. Battaglia, S. M. De Nicolás, S. De Wolf, X. Yin, M. Zheng, C. Ballif, and A. Javey, Appl. Phys. Lett. **104**, 113902 (2014).
[14]C. Battaglia, X. Yin, M. Zheng, I. D. Sharp, T. Chen, S. Mcdonnell, A. Azcatl, C. Carraro, B. Ma, R. Maboudian, R. M. Wallace, and A. Javey, Nano Lett. **14**, 967 (2014).
[15]M. Bivour, J. Temmler, H. Steinkemper, and M. Hermle, Sol. Energy Mater. Sol. Cells **142**, 34 (2015).
[16]J. Bullock, A. Cuevas, T. Allen, and C. Battaglia, Appl. Phys. Lett. **105**, 232109 (2014).
[17]M. T. Greiner, L. Chai, M. G. Helander, W. M. Tang, and Z. H. Lu, Adv. Funct. Mater. **22**, 4557 (2012).
[18]M. T. Greiner, L. Chai, M. G. Helander, W. M. Tang, and Z. H. Lu, Adv. Funct. Mater. **23**, 215 (2013).
[19]J. Geissbühler, J. Werner, S. Martin De Nicolas, L. Barraud, A. Hessler-Wyser, M. Despeisse, S. Nicolay, A. Tomasi, B. Niesen, S. De Wolf, and C. Ballif, Appl. Phys. Lett. **107**, 081601 (2015).
[20]M. Bivour, B. Macco, J. Temmler, W. M. M. (E.). Kessels, and M. Hermle, Energy Procedia **92**, 443 (2016).
[21]B. Macco, M. F. J. Vos, N. F. W. Thissen, A. A. Bol, and W. M. M. Kessels, Phys. Status Solidi RRL **9**, 393 (2015).
[22]J. Yu, Y. Fu, L. Zhu, Z. Yang, X. Yang, L. Ding, Y. Zeng, B. Yan, J. Tang, P. Gao, and J. Ye, Sol. Energy **159**, 704 (2018).
[23]J. Tong, Y. Wan, J. Cui, S. Lim, N. Song, and A. Lennon, Appl. Surf. Sci. **423**, 139 (2017).
[24]L. Neusel, M. Bivour, and M. Hermle, Energy Procedia **124**, 425 (2017).
[25]B. Demaurex, S. De Wolf, A. Descoeudres, Z. Charles Holman, and C. Ballif, Appl. Phys. Lett. **101**, 171604 (2012).
[26]L. Gerling, S. Mahato, C. Voz, R. Alcubilla, and J. Puigdollers, Appl. Sci. **5**, 695 (2015).
[27]N. Alov, J. Surf. Invest. X-Ray, Synchrotron Neutron Tech. **8**, 247 (2014).
[28]T. J. Driscoll, L. D. McCormick, and W. C. Lederer, Surf. Sci. **187**, 539 (1987).
[29]R. H. Cox and H. Strack, Solid State Electron. **10**, 1213 (1967).
[30]B. Hoex, S. B. S. Heil, E. Langereis, M. C. M. Van De Banden, and W. M. M. Kessels, Appl. Phys. Lett. **89**, 042112 (2006).
[31]J. G. Choi and L. T. Thompson, Appl. Surf. Sci. **93**, 143 (1996).
[32]M. F. J. Vos, B. Macco, N. F. W. Thissen, A. A. Bol, and W. M. M. (Erwin) Kessels, J. Vac. Sci. Technol. A **34**, 01A103 (2016).
[33]F. Werfel and E. Minni, J. Phys. C **16**, 6091 (1983).
[34]D. O. Scanlon, G. W. Watson, D. J. Payne, G. R. Atkinson, R. G. Egdell, and D. S. L. Law, J. Phys. Chem. C **114**, 4636 (2010).
[35]L. Salvatl, L. E. Makovsky, J. M. Stencel, F. R. Brownls, and D. M. Hercules, J. Phys. Chem. **85**, 3700 (1981).
[36]A. P. Shpak, A. M. Korduban, M. M. Medvedskij, and V. O. Kandyba, J. Electron Spectrosc. Relat. Phenom. **156–158**, 172 (2007).
[37]J.-C. Dupin, D. Gonbeau, P. Vinatier, and A. Levasseur, Phys. Chem. Chem. Phys. **2**, 1319 (2000).
[38]O. Akhavan, R. Azimirad, S. Safa, and E. Hasani, J. Mater. Chem. **21**, 9634 (2011).
[39]M. C. Biesinger, B. P. Payne, A. P. Grosvenor, L. W. M. Lau, A. R. Gerson, and R. S. C. Smart, Appl. Surf. Sci. **257**, 2717 (2011).
[40]M. Vasilopoulou, I. Kostis, N. Vourdas, G. Papadimitropoulos, A. Douvas, N. Boukos, S. Kennou, and D. Davazoglou, J. Phys. Chem. C **118**, 12632 (2014).
[41]S. Salimian and M. Delfino, J. Appl. Phys. **70**, 3970 (1991).
[42]T. Zhang, C. Lee, B. Gong, and S. Lim, J. Vac. Sci. Technol. A **36**, 1 (2018).
[43]M. Vasilopoulou, A. Soultati, D. G. Georgiadou, T. Stergiopoulos, L. C. Palilis, S. Kennou, N. A. Stathopoulos, D. Davazoglou, and P. Argitis, J. Mater. Chem. A **2**, 1738 (2014).
[44]V. Naumann, M. Otto, R. B. Wehrspohn, M. Werner, and C. Hagendorf, Energy Procedia **27**, 312 (2012).
[45]J. P. Ponpon and B. Bourdon, Solid State Electron. **25**, 875 (1982).
[46]A. Borgschulte, O. Sambalova, R. Delmelle, S. Jenatsch, R. Hany, and F. Nüesch, Sci. Rep. **7**, 40761 (2017).
[47]K. B. Koller, W. A. Schmidt, and J. E. Butler, J. Appl. Phys. **64**, 4704 (1988).
[48]C.-Y. Lee, M. I. A. Aziz, S. Wenham, and B. Hoex, Jpn. J. Appl. Phys., Part 1 **56**, 08MA08 (2017).